



Support on Deformation Failure of Layered Soft Rock Tunnel Under Asymmetric Stress

Xiaojie Yang¹ · Wei Ming^{1,2} · Weiran Zhang^{1,2} · Chun Zhu³ · Yadong Mao^{1,2} · Xiang Wang^{1,2} · Manchao He¹ · Zhigang Tao^{1,2}

Received: 23 April 2022 / Accepted: 16 August 2022 / Published online: 6 September 2022
© The Author(s), under exclusive licence to Springer-Verlag GmbH Austria, part of Springer Nature 2022

Abstract

The Muzhailing tunnel is located in the plateau and mountainous areas. Under the combined action of strong earthquakes, large fault zones and dense and huge tectonic stresses, the weak surrounding rock of the tunnel is usually fissured. Repeated, irregular and asymmetric large deformation and damage accidents often occur during the construction process. To explore the asymmetric large deformation and failure characteristics of the surrounding rock caused by asymmetric stress, this paper considers the equal straight wall arch tunnel as the research object and explores the deformation mechanism of a carbonaceous slate tunnel under asymmetric stress by applying the physical model experiment. Initially, based on the actual geometric characteristics, spatial distribution characteristics and engineering geological conditions of the tunnel, the optimal similarity ratio is determined, and the tunnel physical model under asymmetric stress is established. Afterward, by analyzing the variation laws of displacement, surrounding rock strain anchor cable axial force under asymmetric load, the deformation mechanism of the tunnel surrounded by carbonaceous slate under asymmetric load is revealed. The influence mechanism and control countermeasures of asymmetric stress on the tunnel surrounded by carbonaceous slate are explored by integrating the macro failure characteristics and failure forms of the tunnel. Finally, the 1G-NPR anchor cable characterized by constant resistance and large deformation with a negative Poisson's ratio and the 2G-NPR bolts with long and short combination support are selected to propose control measures for carbonaceous slate tunnels affected by asymmetric stress. The asymmetric support measures are verified by on-site support tools. The research results indicate that with the loading of asymmetrical stress, obvious asymmetrical deformation occurs in the carbonaceous slate tunnel model due to stress concentration, such as bending deformation, block falling and surface peeling of the sidewall and the bottom. The deformation can be effectively controlled by a combination of long and short bolts and cables, which provides a theoretical basis and practical guidance for the design of tunnel asymmetric support with a similar engineering background.

✉ Zhigang Tao
taozhigang1981@163.com

Xiaojie Yang
yxjcumt@163.com

Wei Ming
mingweicumtb@163.com

Weiran Zhang
149521237@qq.com

Chun Zhu
zhu.chun@hhu.edu.cn

Yadong Mao
maoyd2020@163.com

Xiang Wang
Wx790452186@gmail.com

Manchao He
94773308@qq.com

¹ State Key Laboratory for Geomechanics and Deep Underground Engineering, Beijing 100083, China

² School of Mechanics and Civil Engineering, China University of Mining and Technology-Beijing, Beijing 100083, China

³ School of Earth Sciences and Engineering, Hohai University, Nanjing 210098, China

Highlights

- The failure in the study area represents a parallel or small angle oblique fault mode, leading to severe, non-uniform pressure failure.
- The sudden increase of the axial force of the monitoring anchor bolt can be used as a monitoring and early warning tool for detecting tunnel deformations.
- The effect of 2G-NPR large deformation bolt support in controlling asymmetric large deformation failure of tunnel is verified on the geomechanical model experiment and field.

Keywords Asymmetric deformation · Soft rock tunnel · Physical model experiment · Fault structure · 2G-NPR bolt

1 Introduction

During the construction and operation stages of tunnels built in China and abroad, it is usually difficult to predict and control the large asymmetric deformation of the tunnel surrounding rock mass. This has attracted considerable attention from researchers working in this field. Unpredictable asymmetric damage disasters are frequently encountered during the construction, operation, and maintenance stages, which are caused by several factors, such as the manual excavation deflection of the soft rock in tunnels (Grew 1974; Zheng et al. 2022), the extrusion rock mass deformation (Aydan et al. 1993; Zhang et al. 2012), the landform (Lei et al. 2015), the lithology of the surrounding rock mass, the structural and the various comprehensive asymmetric deformations during the operation and maintenance stages (Liu et al. 2022; Sun et al. 2019). If the surrounding rock mass of the tunnel is deformed and damaged asymmetrically, it will critically endanger the safety and regular use of the tunnel.

This asymmetric failure problem has sparked great interest for national and foreign researchers. The mechanical properties of the underground cavern structure and the asymmetric large deformation failure mechanism of the surrounding rock mass and the tunnel excavation are studied by applying theoretical research, physical simulation experiments, and numerical simulations. Vitali et al. (2019) studied the axial displacement and the axial shear stress under the action of the far-field shear stress and concluded that the analytical solutions of the principal stress on the elastic foundation are inconsistent with the shallow buried tunnel. Chen et al. (2019) and Yang et al. (2017) analyzed the influence of the shear coupling effect between the layered soft rock and the joint plane. In addition, they investigated the interaction of parallel joints on the mechanical behavior of the jointed rock mass model through the asymmetric deformation of the surrounding rock mass and the cracking of the secondary lining. Xiong et al. (2020) and Zhang et al. (2020) examined the asymmetric characteristics of the roadway top, floor, and the left and right sides by combining

theoretical analysis and numerical simulations according to the asymmetric deformation and failure characteristics of the roadway surrounding rock mass in the mining area. The obvious asymmetric deformation during the tunnel excavation process was studied using the physical model test, and its failure mechanism and mechanical properties, such as the bottom drum, were analyzed (Sun et al. 2017, 2018; Yang et al. 2018; Guo et al. 2021; Zheng et al. 2022). Lin et al. (2018) studied the asymmetric deformation and the cracking characteristics of dam abutment using three model tests of the Jinping arch dam. Zheng et al. (2021) applied the geomechanical model test and the numerical analysis to study the mechanical properties of the middle soil pillar (MSP) soil column between asymmetric dense parallel tunnels. The results indicate that the final damage mode of the MSP is asymmetric. Liu et al. (2021) investigated the scale test of different bias voltages, the lining crack evolution process, and the cracking mechanism caused by bias voltage by XFEM. To research the asymmetry of the supporting structure caused by the local topography and the bedding structure during construction. Chen et al. (2020) and Peng et al. (2021) studied the asymmetric instability of kilometers deep roadway with different lithologies using the acoustic emission signal of the in-situ rock and the three-dimensional in-situ stress. In addition, they examined the shallow tunnel, the soft rocks, the landslide sediments passing through the fault zone, and the deep tunnel passing through the soft and the hard rocks. To clarify the damage caused by the large deformation of the surrounding rock mass to the underground caverns, Chen et al. (2020a, b) and Yu et al. (2020) proposed strengthening the stability of the roadway surrounding rock mass with the constant resistance large deformation bolt (CRLB), while Tao et al. (2021) suggested using the NPR anchor cable to prevent the large-scale overturning instability failure of the layered upward slope.

In the study of the asymmetric failure mechanism of tunnel surrounding rock, Chen (1982) found that the large deformation of roadway surrounding rock is closely related to the complicated geological structure. Aydan et al. (1993)

investigated rock squeezing tunnels in Japan and found that the extrusion deformation of roadway surrounding rock was slow and gradual. Wang et al. (2009) studied the Wushaoling tunnel in China and concluded that stress-induced dilatancy of surrounding rocks led to the deformation. Zhao et al. (2019) studied the degradation, softening, and expansion of carbonaceous slate resulting from groundwater during construction, caused large deformation failure in the bottom structure of the carbonaceous slate tunnel directly. Guo et al. (2021) analyzed the large deformation failure of the layered tunnel in Minxian county with the help of the geomechanical Model Experiment. The available literature on the asymmetric failure mechanism of tunnel surrounding rock primarily focuses on the impact of shallow tunnel conditions (such as topography, landform, and disturbance) and the physical and mechanical parameters of surrounding rock lithology (such as the influence of groundwater on soft rock).

Limiting large asymmetric deformation and ensuring the safety and stability of the tunnel is a research topic worthy of attention researchers. Lei et al. (2015) studied the variation law and failure mechanism of surrounding rock stress of shallow buried tunnels under asymmetric load. They proposed that targeted support measures should be taken by closely monitoring the development of the morphological characteristics of the lining structure during tunnel construction. Hu et al. (2020) studied the shield tunnel passing through the jointed rock mass. To limit the asymmetric deformation of jointed rock mass, the method of adding anchor cable and reinforcing grouting was proposed. Qi et al. (2020) put forward the control method of strengthening asymmetric coupling support for asymmetric problems. Wu et al. (2020) used long anchor cables to restrain the serious asymmetric deformation of the roadway and utilized short cables and closed U-shaped steel to improve the in-situ stress state of the roadway caused by mining. Ta et al. (2021) proposed a collaborative control technology of roof cutting for pressure relief and support strengthening based on the asymmetric deformation mechanism of the coal mining roadway. Chen et al. (2021) studied the influencing factors of asymmetric deformation of surrounding rock in the deep roadway and adjusted the surface deformation of surrounding rock by improving the closed support scheme to make the asymmetric deformation close to the symmetrical distribution. Xu et al. (2021) put forward a control strategy based on asymmetric high prestressed truss anchor cable to address the asymmetric deformation of surrounding rock caused by strong mining. Although there has been no significant advancement in new support materials, the traditional bolt/cable support system is still used for asymmetric support. Under the influence of macrostructure and strength parameters of surrounding rock, there is still a lot of research space for the new bolt cable support system with asymmetric failure.

By selecting the ventilation duct of the Muzhailing tunnel 2# inclined shaft as the study area, this paper proposes the

physical model of the tunnel surrounded by carbonaceous slate based on the similarity theory. Besides, it carries out the physical model test of the single-side fault tunnel under asymmetric stress. This paper reveals the deformation mechanism of the carbonaceous slate surrounding the rock tunnel under asymmetric load by analyzing the variation laws of displacement, surrounding rock stress, and anchor cable axial force under asymmetric load. In addition, by combining the obtained data with the macro failure characteristics and the failure forms of the tunnel, this paper explores the influence mechanism and the control countermeasures of asymmetric stress on the tunnel surrounded by a carbonaceous slate. In addition, it verifies the asymmetric support countermeasures by field application to provide a theoretical basis and practical guidance for designing asymmetric support for tunnels with a similar engineering background.

2 Geological Engineering Conditions

2.1 Formation Lithology and Geological Structure

The primary lithology of the tunnel surrounding rock mass is represented by a moderately weathered carbonaceous slate characterized by horizontal stratification. The thickness of the slate beds varies between 4 and 20 cm. The dip angle is affected by the structural fault zone. During the sampling process, the surrounding rock was identified as highly fragmented and belonged to the class V type surrounding rock. In addition, under the influence of strong active faults, the fault phenomenon is further intensified to form the influence area of the fault fracture zone (Fig. 1).

The Muzhailing 2# inclined shaft tunnel is located at the intersection of multiple active tectonic plates and is characterized by strong seismic activity (Fig. 2). The fault structural zones are dense and large, while the small faults are staggered. The small fault fracture zones are clustered, and the influence range of the fault zones is wide. The self-stability ability of the surrounding rock is poor. Due to the combined action of the Himalayan movement and the Yanshan paleo movement, a unique geological environment was created. The surrounding rock mass of the tunnel is represented by carbonaceous slates and weathered sandstones with intercalations of carbonaceous slates. Occasionally, strongly weathered sandstones can be distinguished among the predominant lithologies.

2.2 Initial In-Situ Stress

The construction orientations show the NWW and EW, and the maximum principal stress is the NNE orientation. The maximum horizontal principal stress is greater than the minimum horizontal principal stress, and both are higher

than the vertical stress. After performing the calculations, the ratio between the rock uniaxial compressive strength to the maximum in-situ stress is less than 4, as indicated in Table 1. The in-situ stress in this area can be attributed to the extra high ground stress category.

2.3 Physical and Mechanical Properties of the Surrounding Rock

The SC-300 automatic coring machine was utilized to process the standard specimen of the carbonaceous slate sample, while the uniaxial compressive strength and various physical parameters were measured using the 2000 kN indoor uniaxial triaxial system. The results of the uniaxial compression test are shown in Table 2.

Low strength, strong expansibility, and easy deformation define the surrounding rock. The development of the surrounding rock joints is irregular, and the degree of fragmentation is high. The strength of the specimens selected for analyses is high, resulting in 4 groups of splitting failure and a group of shear failure. However, the actual situation should be that most of them are characterized by shear failure. By analyzing the microstructure features (Fig. 3), it must be considered that the microstructure plane also presents a thin layer, indicating a good “self-similar characteristic”.

3 Geomechanical Model Tests

3.1 Similar Simulation Parameter Design and Material Test

3.1.1 Parameter Test of the Carbonaceous Slate and Simulation Material

This study considers the left air duct section of the Muzhailing tunnel 2# inclined shaft as the research object. The shape of the tunnel is a straight wall circular arch. The widest part

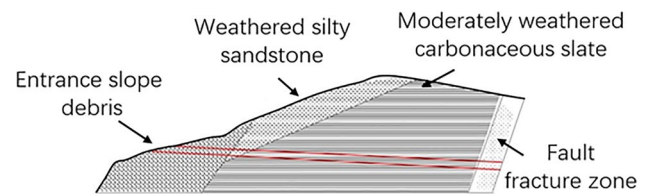


Fig. 1 Schematic diagram of the 2# inclined shaft crossing the rock strata

of the tunnel is 7756 mm, the height is 8090 mm, and the radius of the circular arch is 4000 mm. The bedding angle of the rock mass varies between 0 and 30°. Multiple horizontally stratified rock layers represent geological succession. The surrounding rock is classified as grade V engineering rock mass. The predominant lithology is a moderately weathered carbonaceous slate with rare intercalations of strongly weathered sandstone. Its structure is characterized by a lamellar structure with high joint development, as illustrated in Fig. 4.

According to the similarity theory, the geometric similarity constant is 26, and the density similarity ratio is 0.57. Therefore, the thickness of the slate model will be controlled by 1.5–10 mm. The physical and mechanical properties of the surrounding rock prototype are indicated in Table 3.

The primary preparation materials are river sand, barite powder, gypsum, and water. The mix proportion is illustrated in Table 4. Indoor uniaxial compressive strength tests were performed on each sample to obtain the uniaxial compressive strength curve, as shown in Fig. 5.

3.1.2 Experiment on the Mechanical Properties of the NPR Simulated Materials

This experiment selects the 1G-NPR anchor cable and the 2G-NPR bolt as new support materials. Figure 6 illustrates the support working principle of the 1G-NPR anchor cable and the 2G-NPR bolt. The working principle of the 1G-NPR anchor cable primarily depends on the movement of the

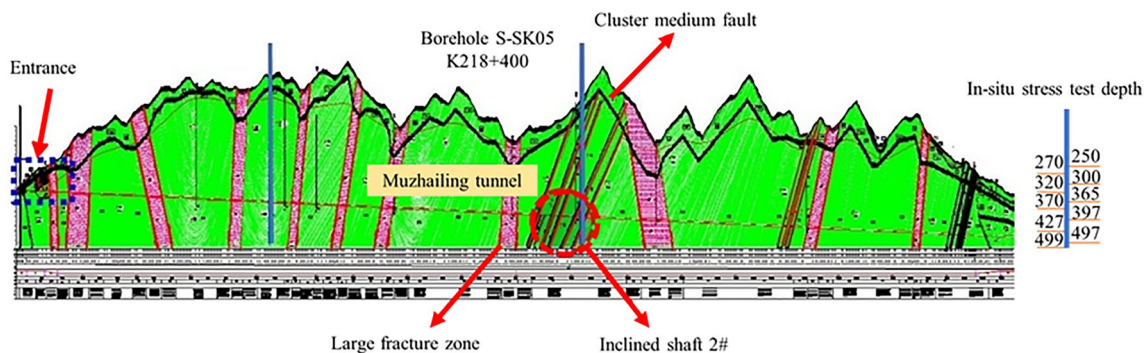


Fig. 2 Geological section of the Muzhailing tunnel

Table 1 Ratio of in-situ stress and R_c for the Muzhailing tunnel

No	Test depth (m)	S_H/MPa	R_c/MPa	R_c/MPa
1	250	11.37	20–30	1.76–2.64
2	270	12.14	20–30	1.65–2.47
3	300	11.37	20–30	1.76–2.64
4	320	14.93	20–30	1.34–2.01
5	365	14.84	20–30	1.35–2.02
6	370	12.98	20–30	1.11–1.67
7	397	16.28	20–30	1.23–1.84
8	427	18.76	20–30	1.07–1.60

constant resistance body to obtain the negative Poisson's ratio effect in the macro dimension of the structure. The 2G-NPR bolt is uniformly deformed by the tension of its material and can withstand significant deformations. When the deformation of the surrounding rock reaches the limit value, the load it bears is lower than its limit bearing capacity to achieve the final stable support. During the tension process, the Poisson ratio is small, and there is no yield platform. The strain value is not less than 0.2, with high strength, tensile fracture, and no noticeable necking effect. It can be observed from Fig. 7 that the static tensile curve of the 2G-NPR bolt includes the elastic deformation period, the constant resistance stage, and the failure stage, while the static tensile curve of the 1G-NPR anchor cable contains the elastic deformation period, the plastic strengthening stage and the failure stage. The remarkable feature is that the area surrounded under all tensile curves has a rectangular or approximately rectangular shape. This study uses the micro bolt model with the same working principle and tensile characteristics as the 2G-NPR bolt to support the experimental model. According to the load similarity ratio $C_F = C_\rho C_l^3 = 0.57 \times 26^3 \approx 10,000$, aluminum wire, iron wire, tin wire, and other simulated materials were selected for the tensile test. Based on the geometric and mechanical similarity, the solder wire with a diameter of 1.2 mm and a length of 150 mm is selected to simulate the 2G-NPR anchor rod with a length of 3900 mm and a breaking force of 230 kN. The solder wire with a diameter of 1.8 mm and a length of 300 mm is chosen to imitate the 1G-NPR anchor cable with a length of 7800 mm and a constant resistance force of 350 kN.

3.2 Principle of the Experimental System and the Monitoring Equipment

The asymmetric stress application device is designed and manufactured based on the static vector synthesis principle (Fig. 8) to carry out the asymmetric stress release simulation similar to the prototype engineering case. In addition, the application device is tightly fixed in the upper right corner of the model loading frame through rigid bolts. The device is made of high-strength steel assembled by

Table 2 Results of the uniaxial compression test

No	Modulus of elasticity E/GPa	Average value/ GPa	Poisson's ratio μ	Average value μ	Uniaxial compressive strength σ_c/MPa	Average value /MPa	Failure characteristics
S1	11.5	11.22	0.15	0.154	74.8	74.0	Split
S2	10.8		0.18		76.9		Shear
S3	12.1		0.16		72.1		Split
S4	10.5		0.13		75.2		Split
S5	11.2		0.15		71.0		Split

Fig. 3 Self-similarity of the micro-thin layer structure

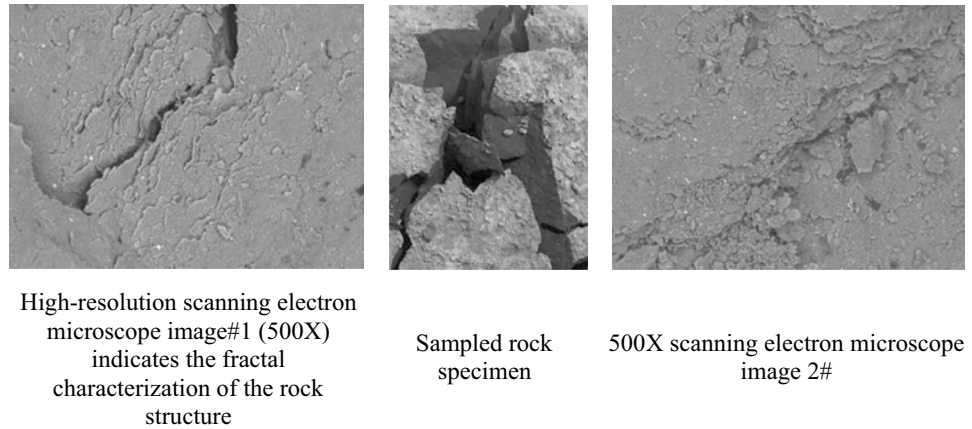
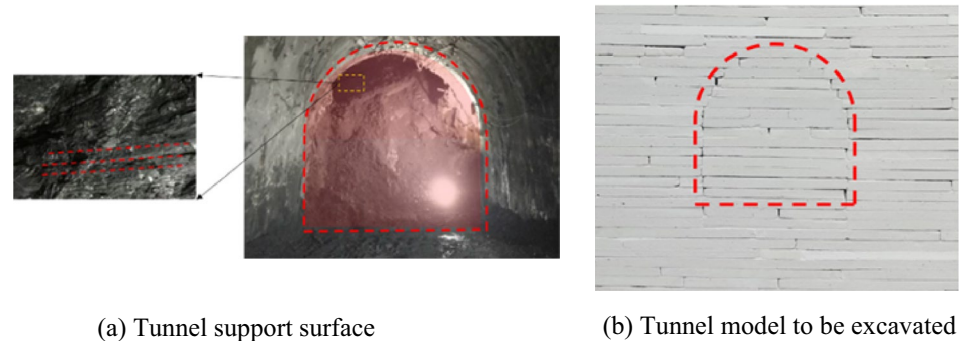


Fig. 4 Geometric similarity model



welding, and its shape is an isosceles right-angled triangle. Its upper part is connected to the steel column heads of the first two groups of loaders from right to left with U-shaped bolts. Six steel rollers are installed on the right side and closely fit with the first two groups of steel column heads of the right loading frame through the steel backing plate. The four groups of hydraulic column heads

at the upper right corner slowly extend when the load is applied through the high-precision static servo-hydraulic console. When the inclined edge of the loading device is about to contact the model body, the inclined edge base plate is added to increase the contact area to prevent the steel frame from penetrating the soft model body. The static force is transmitted through the loading device to

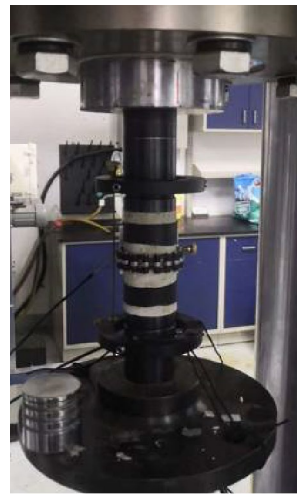
Table 3 Physical and mechanical parameters of the prototype and model

Main lithology	Uniaxial compressive strength/MPa	Poisson's ratio μ	Gravity γ /kN/m ³	Modulus of elasticity E /GPa
Carbonaceous slate	29–29.5	0.154	26.85	11.22
Similar model materials	1.96–2.02	0.154	15.30	0.757

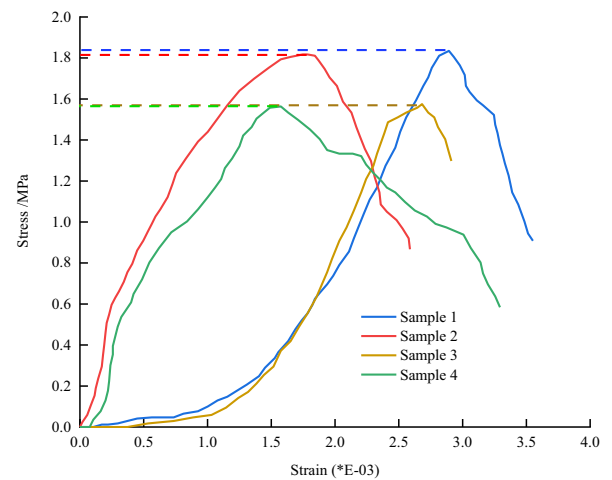
Table 4 Ratio of similar simulated materials for the surrounding rock

Sample no	Total mass/kg	River sand/kg	Barite powder/kg	Gypsum/kg	water/kg	Forming state	Simulated material
Sample 1	1.00	0.200	0.550	0.130	0.120	Forming	Surrounding rock
Sample 2	1.00	0.180	0.570	0.130	0.120	Forming	Surrounding rock
Sample 3	1.05	0.155	0.600	0.140	0.110	Forming	Initial shotcrete C25
Sample 4	1.02	0.142	0.600	0.150	0.110	Forming	Secondary lining concrete C30
Sample 5	1.02	0.180	0.600	0.142	0.098	Unformed	/
Sample 6	1.00	0.190	0.600	0.140	0.070	Unformed	/

Fig. 5 Uniaxial compressive strength experiments on the simulated materials



(a) Uniaxial compression system



(b) The obtained stress-strain curves

realize the asymmetric static force application using the application and synthesis of the upper and the right pressure. Simultaneously, the displacement and deformation of the surrounding rock are collected by the digital speckle displacement and deformation field test system.

3.3 Experimental Scheme

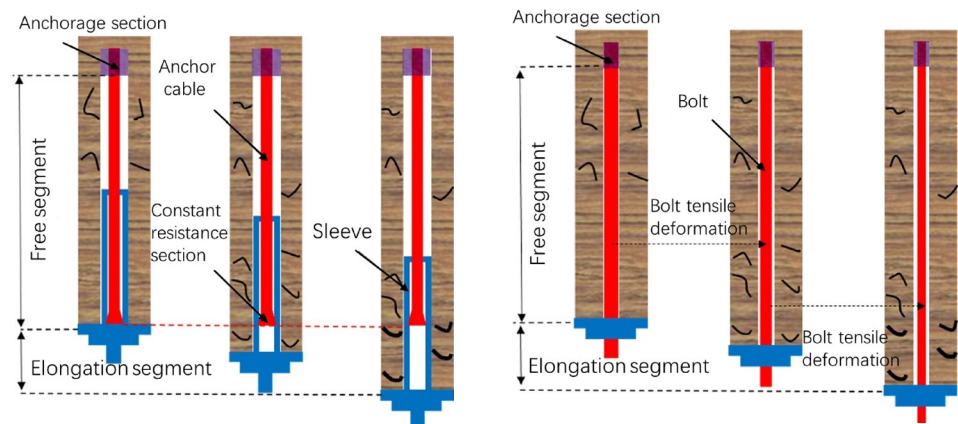
A BW resistance strain earth pressure sensor and a BF120-3BA biaxial right angle strain rosette are used for the monitoring process. The design of monitoring points is illustrated in Fig. 9. The anchor/cable is used as the support mechanism to study the failure of the model during the support state. At the same time, the anchor cable is required to have control and monitoring characteristics. AC1, AC3, and AC5 with a length of 300 mm are considered 1G-NPR anchor cables, while the others with a length

of 150 mm are 2G-NPR bolts. The support monitoring scheme is shown in Fig. 10.

The hydraulic device is loaded with simulated confining pressure in this model test. The maximum vertical in-situ stress of the buried depth can reach 12.50 MPa, while the maximum horizontal principal stress is 21.00 MPa. The stress similarity ratio of the test model is 15, the vertical load is 0.83 MPa, and the horizontal load is 1.40 MPa. The initial asymmetric load is equal to 2.0 MPa and gradually increases until it reaches the overload failure state. Load application parameters are indicated in Table 5.

The stress loading path of this test can be divided into three stages: (1) load the vertical and the horizontal stress to the initial stress state, (2) stabilize the existing pressure, excavate the tunnel according to the preset excavation line through a one-time excavation procedure of the whole section, and add an anchor bolt/anchor cable and lining support after clearing the sundries, (3) asymmetric stress is applied to the model failure, as illustrated in Fig. 11. Stage

Fig. 6 Working principle of the anchor cable with constant resistance



(a) 1G-NPR anchor cable support principle

(b) 2G-NPR bolt support principle

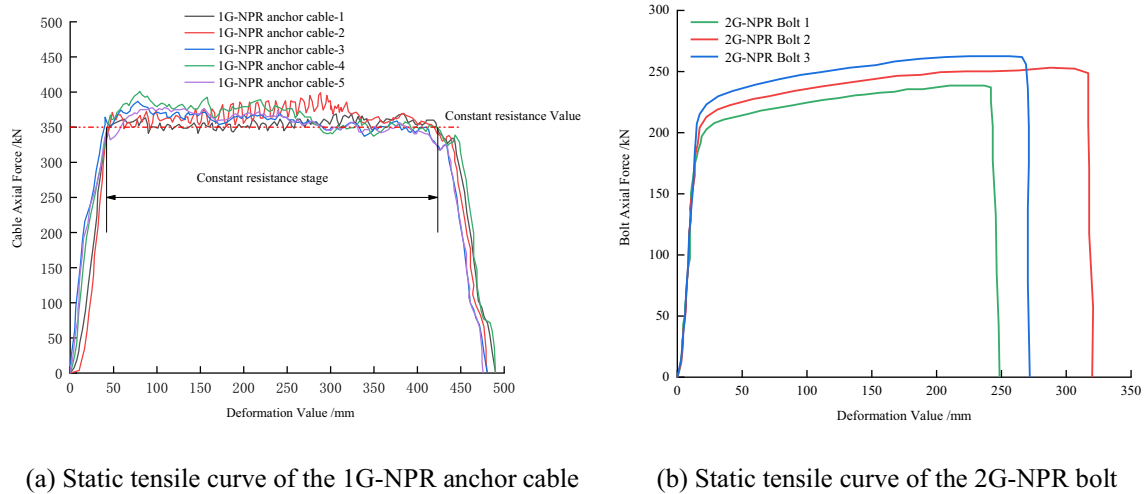


Fig. 7 Mechanical characteristics of the anchor cable/bolt

A represents the excavation stage, and stage B is the stage, where asymmetrical stress is implemented. (Note: the vertical stress curve coincides with the horizontal stress curve before the 0–80 min time interval).

4 Results

4.1 Macroscopic Deformation Characteristics

The entire loading process is divided into three stages, and the macro failure characteristics of each loading stage are illustrated in Fig. 12.

Initially, the unit plates were preloaded so that they were compacted and stable for 20 min after each loading stage. The deformation of the surrounding rock near the cavern is shown in Fig. 12 (stage A). A few tension cracks appeared in the unit plate when the load reached the A4 stage.

After that, during the stage B loading process, the stable pressure was maintained horizontally and vertically, and a rapid one-time full-face excavation was carried out. The deformation of the cavern is illustrated in Fig. 12 (stage B). Figure 12d indicates the moment after the excavation is completed. At this time, the roof had a large tensile crack (1.6 mm width) on one side of the free face of the arch crown due to excavation, accompanied by a collapse trend, and there was no obvious deformation on the left and the right sides. Figure 12e shows that when the excavation

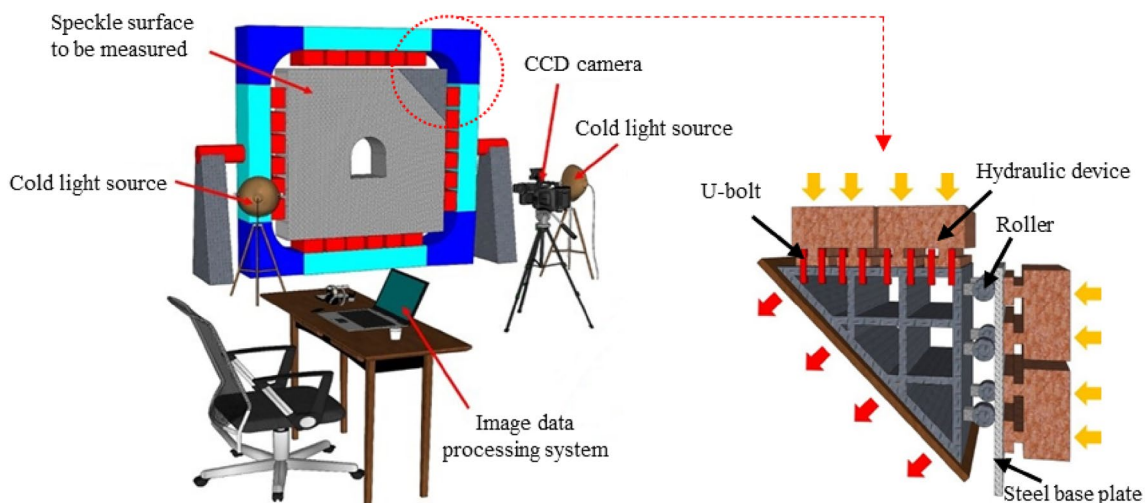


Fig. 8 Speckle test system components and the non-uniform stress application device

is stable at the 140 min mark, the tension crack begins to expand and leads to the falling of the local roof. The inward horizontal sliding occurred at the free surfaces of the two sides, and most of the unit plates were accompanied by an outward extension trend. Figure 12f indicates that after the bolt/cable support and the lining, a small amount of falling debris appears on the arch crown at the 160 min mark, and no evident deformation continued to occur in other areas. A relatively stable state characterizes the surrounding rock during the entire process.

When the loading stage reaches stage C, the horizontal and vertical pressure stabilization state is extended, the pressure of the loading device is adjusted, the asymmetric external load is applied, and the deformation process of the cavern in the characteristic period of stage C is recorded (Fig. 12).

When the applied asymmetric load reaches 1.6 MPa, the tunnel maintains the phase B shape for 160 min without suffering any damage. The primary anomaly is that loud noise is produced. The actual situation should be that individual

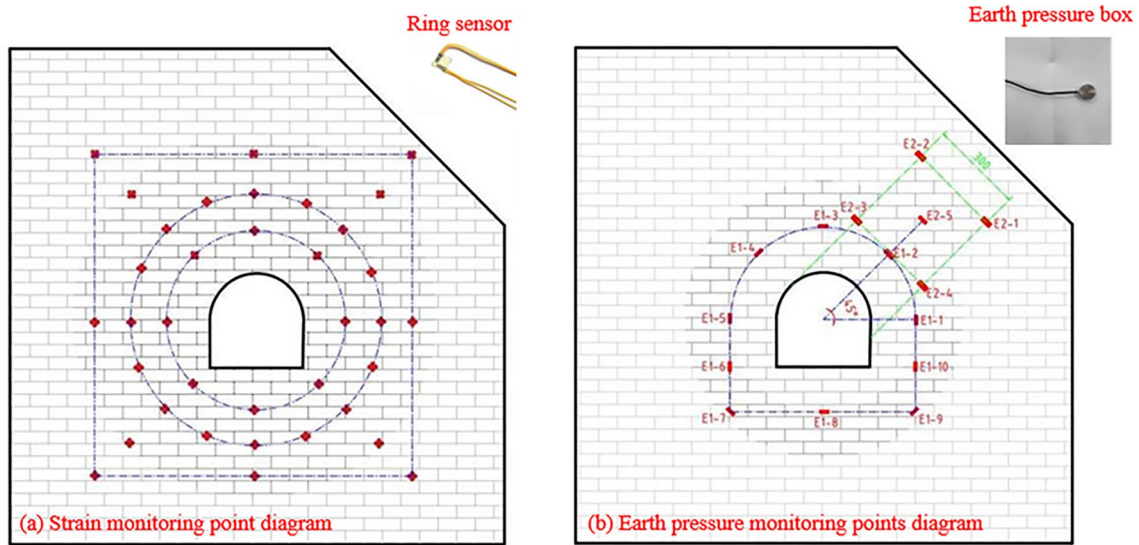


Fig. 9 Tensile pressure and the strain monitoring system

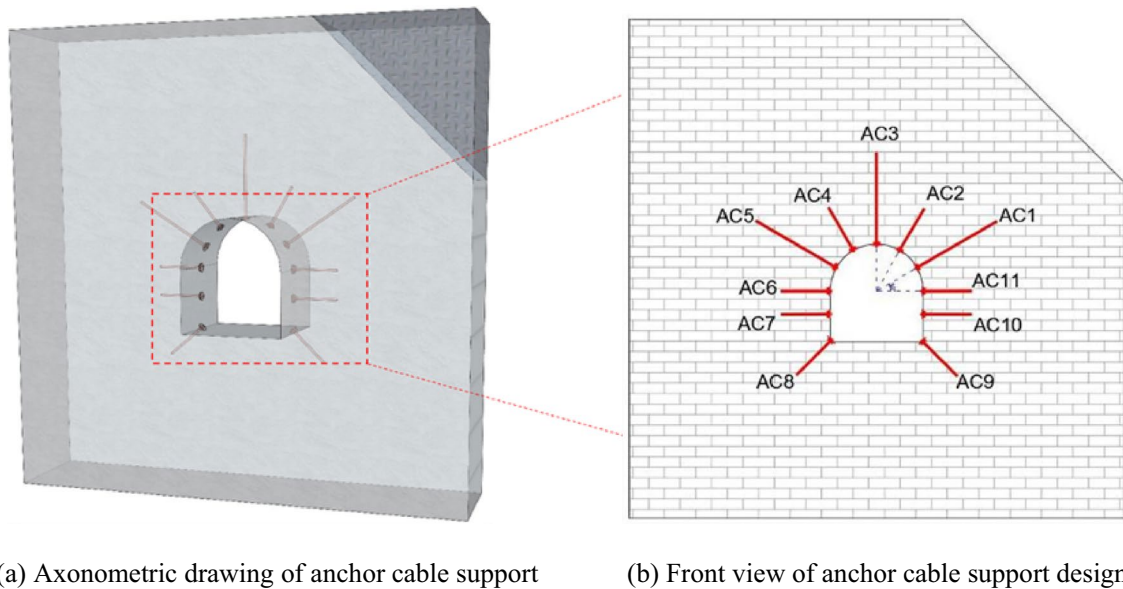
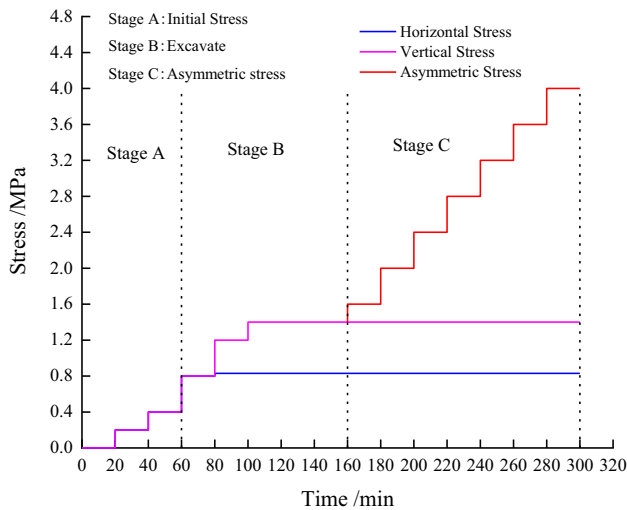


Fig. 10 Anchor cable model support design

Table 5 Stress simulation parameters

Stress category	Vertical stress/ MPa	Horizontal stress/MPa	Asymmet- ric stress/ MPa
Prototype stress	12.50	21.00	30.00
Model stress	0.83	1.40	2.00

**Fig. 11** Three parts of the loading process

plates in the model break and fly dust appear simultaneously. When the applied load reaches 2.0 MPa, i.e., the process is at the 180 min mark in the C2 period, the surrounding rock in the upper right side of the cavern is bent and deformed, and the overall average surrounding rock settlement is measured manually as 6 mm. The rock stratum is broken and bulged with fragments on the right side of the cavern, while the right arch and the sidewall are cracked. The cracks represent the internal spalling caused by the expansion of tension cracks, and there are micro-cracks on the left side of the bottom plate, which tend to bulge upward. The whole model is in a critically unstable state. When the applied load reaches 2.4 MPa, when the process is at the 200 min mark in the C3 period, the overall shape does not change. When the applied load reaches 2.8 MPa, that is, the process is at the 220 min mark in the C4 period, the bending deformation of the surrounding rock in the upper right area of the cavern is intensified, and the average manually measured value of the settlement is 9 mm. In addition, significant spalling failure occurs at the vault, the surrounding overlying rock is separated, several tension cracks appear, multiple roof collapses occur, and the vault and right arch waist have an offset of 5–7 mm from the original contour line. The cracks at the left arch waist and the right arch foot of the tunnel gradually develop and have a continuously increasing trend. At this stage,

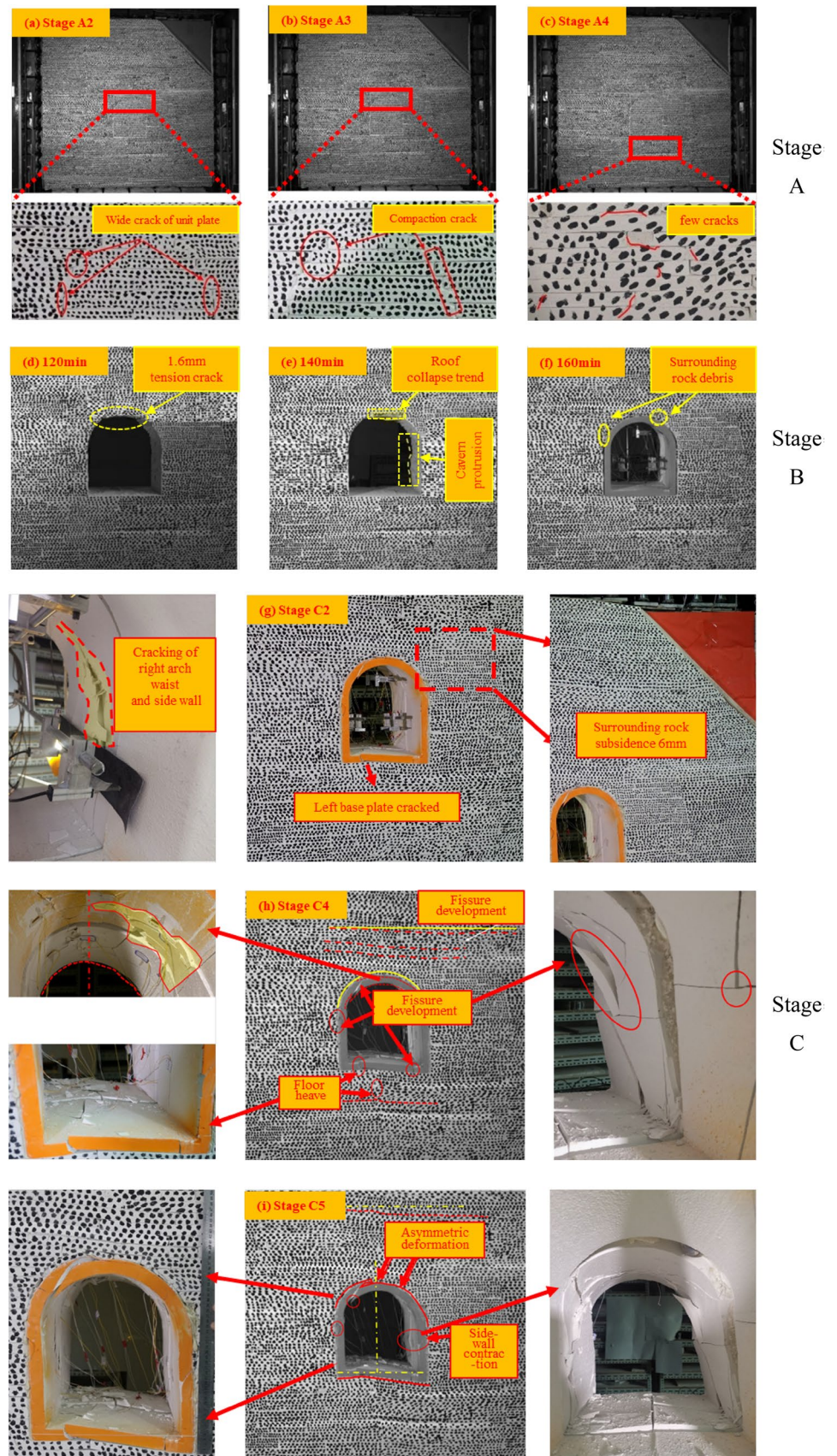
there is an obvious bottom bulge phenomenon. According to the division of the tunnel center line, it can be inferred that there is an obvious bias deformation on the right side, mainly manifested by asymmetric crack distribution and block falling. When the applied load reaches 3.2 MPa, i.e., at the 240–260 min mark in the C5 period, the average deformation of the surrounding rock in the upper right side of the cavern reaches 15 mm, and the spalling failure at the vault is intensified. At the same time, the vault has a horizontal dislocation, and the left and right-side walls shrink inward. In contrast, the right-side wall and arch waist have more pronounced asymmetric deformations, the convergence on the right side of the cavern is significantly higher than on the left side, and distinct unilateral settlement occurs. The manually measured value of the deformation is 13 mm. When the roof and the floor are damaged, it is observed that the deep surrounding rock of the upper and lower free faces is also damaged in the same direction. The bottom heave is seriously damaged at this phase, and the manually measured value is 13 mm. When the applied load reaches 3.6 to 4.0 MPa, severe damage causes the model body to lose its integrity, and an overall collapse occurs.

The analysis indicates that an asymmetric deformation field is generated around the model cavern with the application of asymmetric stress. Initially, the inward sliding of the surrounding rock is generated at one sidewall. Afterward, a tension crack appears on the roof. With the increase of the tension failure on the inner side of the free face, the deflection deformation failure of the roof occurs at the maximum deflection, and the failure area is close to the left side of the cavern. The damage degree of the floor heave is more severe than the roof. First, the floor fracture causes the chain arching of the lower surrounding rock and finally causes the damage of the floor heave to become more significant. With the load increase, the tunnel displays split deformation along the left side of the arch crown and failure of the floor heave. In addition, the deformation on the right side increases, resulting in asymmetric deformation.

In this experiment, the damage evolution process of cracks is primarily represented by the crack incubation stage, the crack propagation stage, and the crack penetration stage, as illustrated in Fig. 13.

Crack incubation stage: before applying asymmetric stress, the cracks in the model body are predominantly unit plate arrangement cracks in the initial construction period. With the subsequent compaction and excavation processes, the number of cracks decreases, while material fractures gradually appear, represented by the crack incubation at the top and the bottom plate. It is mainly the micro crack caused by flexural deformation. The width measured by the feeler gauge is generally 0.05 mm and 0.1 mm, primarily concentrated near the tunnel chamber.

Fig. 12 Deformation process of the surrounding rock in the loading stage



Crack propagation stage: it generally happens at the beginning of the C2 stage, and the small cracks develop into wide cracks. When the crack is created, the stress initially borne by a layer of crack is not in contact, and the stress balance state of the nearby element suddenly changes, resulting in the local ejection fracture of the crack and the secondary fracture of the nearby element plate. The crack width ranges from 1 to 2 mm.

The fracture connectivity stage in the high-density area primarily occurs in the C6 and subsequent stages. Due to the increase of stress, the crack propagates and loosens the whole model structure, and the dense crack is the first part of the penetration region. The connected cracks frequently form a large cavity, resulting in local crushing and silty damage, and finally lead to the collapse of the whole model, which is mainly concentrated between the upper right part of the cavern and the asymmetric stress release point.

By recording the crack propagation process during each stage, it can be observed that the crack propagation mode represents an approximate circumferential range with the tunnel as the center point and gradually moves to an elliptical range toward the upper right side, as illustrated in Fig. 13.

4.2 Displacement Variation Analysis of the Tunnel

The digital image correlation (DIC) processing technology was applied to extract the data points from the stage C instantaneous image of the experimental loading path and

form the change cloud diagram of the global displacement field of the surrounding rock at the specific time points. As indicated in Fig. 14, the horizontal right and the vertical down are designated as the positive direction. (Note: C2.5X represents the displacement in the horizontal direction within the 5 min interval in the C2 stage, and so on).

When the experiment reaches the C2 stage, it is noticeable that the absolute value of the displacement in the horizontal direction is small, which generally remains around the 2 mm mark. It happens in such a manner, because, after applying the horizontal confining pressure and the vertical confining pressure in the early stage, the model achieves the preliminary compaction in the horizontal direction, and the horizontal displacement caused by friction between the unit plates becomes very limited. At the same time, the vertical displacement field in this period shows the bottom drum's emergence or manifestation. The positive and reverse displacement areas are symmetrical around the vertical direction. The positive displacement area spreads and opens from the loading area, while the displacement of the surrounding rock at the bottom plate and the free surface of the bottom plate increases. The bottom drum is about 3 mm at the 20 min mark. At this interval, the damage degree of the surrounding rock is correlated to the occurrence of bottom plate cracks. When the experiment reaches the C4 stage, the absolute value of the horizontal displacement increases and corresponds to an average value of 5 mm. The maximum horizontal displacement is concentrated in the upper area of the cavern, and the lower area is not affected. Simultaneously,

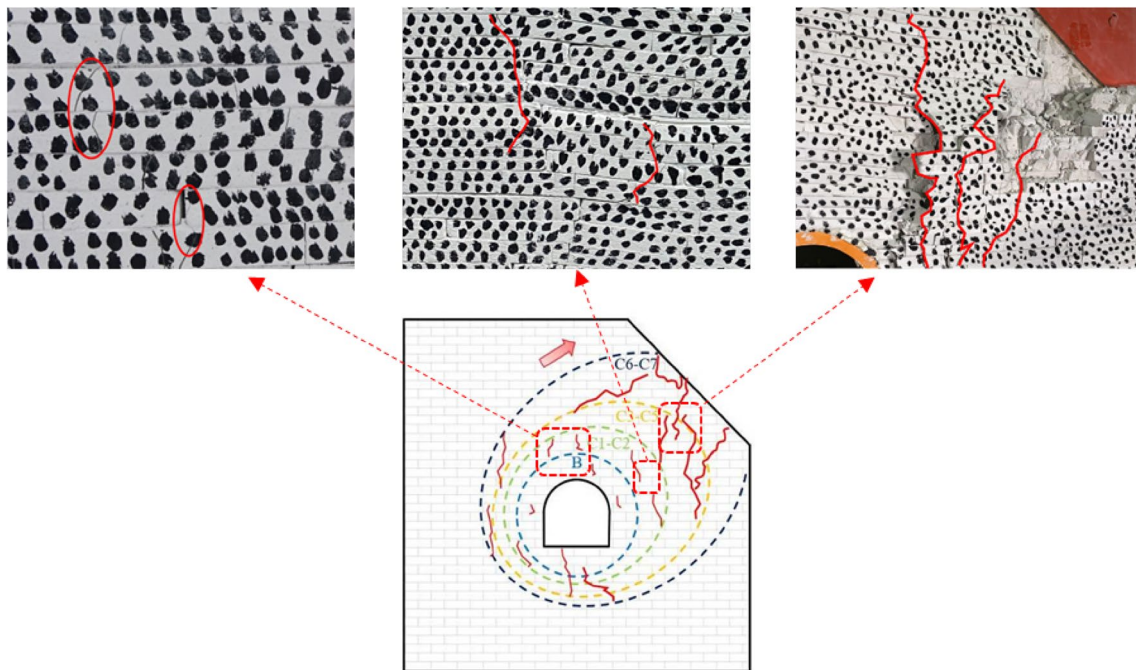


Fig. 13 Fracture damage law and crack propagation characteristics

the vertical displacement increases and reaches an average value of 12 mm. The maximum bottom drum position appears in the left part of the middle of the bottom plate, which is consistent with the measured phenomenon. The maximum vertical displacement value in the upper right corner is 24 mm, and the reverse displacement area shifts to the lower-left corner, which is different from the essential symmetry in the C2 stage. At this interval, prominent asymmetric characteristics are visible. When the experiment reaches the C5 stage, the absolute value of the horizontal displacement increases and reaches an average value of 6 mm. The overall displacement band shows similar characteristics as in the C4 stage. The asymmetric phenomenon of the vertical displacement field intensifies, and the maximum value in the upper right corner is 28 mm. The peak value of the reverse displacement at the bottom plate reaches 15 mm and spreads to the upper left side. At this interval, the large deformation phenomenon of the measured model is consistent.

By analyzing the previously mentioned data, it can be concluded that the phenomena of bias deformation, bottom drum deformation, and unilateral settlement of the model can be explained by the evolution characteristics of the displacement zone. By selecting the horizontal and the vertical directions as examples, the displacement zone is divided into the forward and the reverse displacement zone, that is, the displacement generated by conforming to or against the direction of the reaction force application, as illustrated in Fig. 15.

The horizontal displacement zone is constrained by the lower right part of the cavern, forming the duality of the displacement zone. The vertical displacement zone is divided by the axis passing through the cavern and the radial boundary at the upper right corner. The ray of the displacement zone is symmetrical around the horizontal 30° included angle at the first quadrant. Due to a large number of sudden vibrations in a small area generated by the displacement zone's upper displacement, the model's damaged parts are concentrated near the displacement zone.

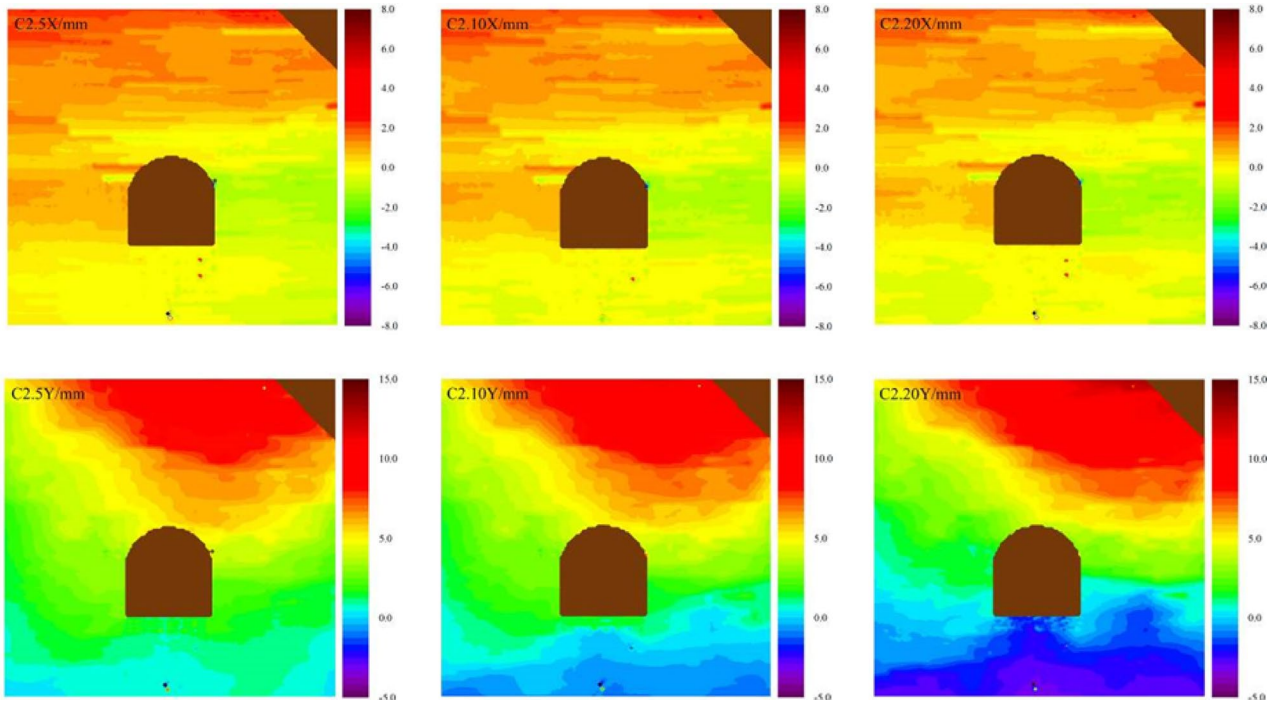
4.3 Displacement Change Analysis of the Tunnel Key Points

As indicated in Fig. 16, the characteristic vital points are selected at the top plate, the bottom plate, the arch waist, and the sidewall of the tunnel. Full-time displacement monitoring and analysis are carried out, and the two-way displacement loading path curve is obtained.

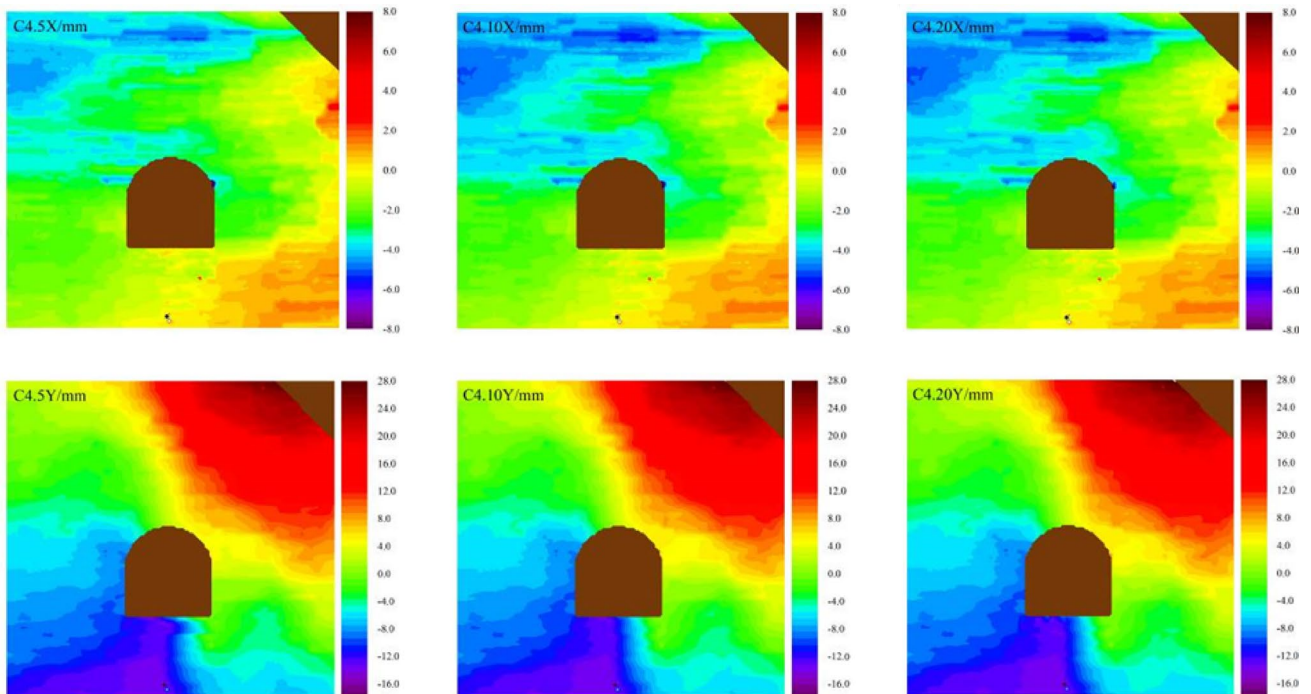
Figure 16a shows the horizontal displacement monitoring curve of the tunnel key points, where the D1–D6 points represent the monitoring points. Since the surrounding rock during the early stage of excavation (stage B) and the initial confining pressure (stage A) are relatively stable with practically no displacement,

the asymmetric loading stage during the late stage of excavation and the subsequent phases are studied. The displacement of the monitoring points slightly fluctuates due to the redistribution of the surrounding rock stress during the late stage of excavation before and after the 160 min mark. When the asymmetric load equal to 1.4 MPa to 1.6 MPa is applied in the C1 stage after the 160 min mark, due to the certain lag of load transmission to the cavern, at the 170 min mark, the displacement of each measuring point begins to develop and gradually widens the gap. Among these, the displacement of the D1 measuring point at the top plate has the fastest variation, while the D4 measuring point at the bottom plate has the slowest variation. When the load is applied, all measuring points form negative displacements, i.e., horizontal right displacement. During the C2–C6 stages, the displacement of the measuring points D1, D2, and D3 are always synchronized and greater than the displacement of other measuring points, while the displacement of the measuring point D4 at the bottom plate always has the smallest values. This phenomenon generates, because the unit plate is staggered primarily by the horizontal driving force, and these three measuring points are located on the right side of the cavern and are vulnerable to the effects of thrust forcers. Therefore, the horizontal boundary restriction at the bottom plate leads to the creation of a small displacement. Each measuring point reaches the horizontal stable state during the C4–C5 stages. With the increase of asymmetric pressure during the C6 and C7 stages, each measuring point enters the critically unstable and complete failure state, and the displacement value suddenly increases.

Figure 16b indicates the vertical displacement monitoring curve of the tunnel key points, where the D1–D6 points represent the monitoring points. When the load is applied, the displacement of each monitoring point shows signs of duality. Accordingly, the displacement values of D1, D2, and D3 are always positive during the C1 stage and after it, indicating that they always move vertically downward, while the displacement values of D4, D5, and D6 are positive before the 195 min and the 210 min marks. Afterward, the values are negative, indicating that they always move vertically upward. This phenomenon occurs when the D1, D2, D3, D4, D5, and D6 points are located on both sides of the displacement zone. At this time interval, the deformation process of the corresponding model body is represented by the asymmetric bottom drum inoculation and the bottom drum deformation. From the C2 to the C6 stage, the absolute value of the displacement at each point increases with the increasing load, and the displacement at each point stabilizes after the C4–C5 stages. The sudden increase of the displacement at the D2 measuring point in the final failure stage indicates that the

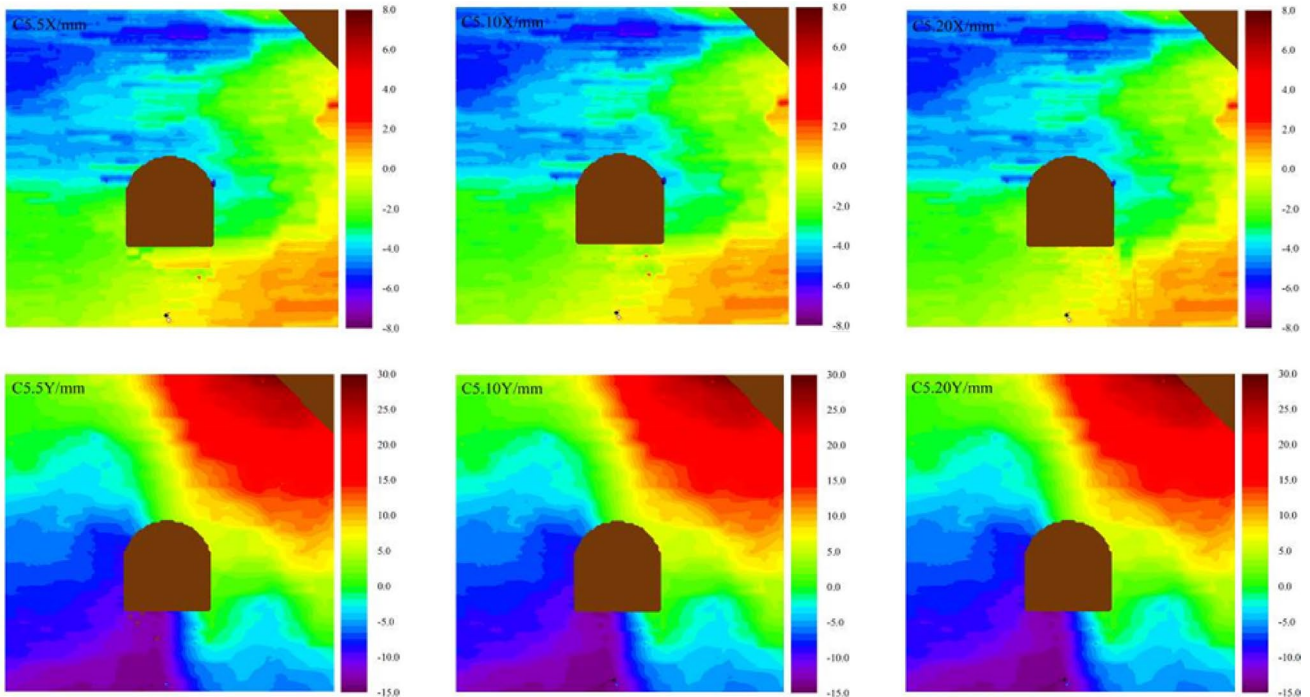


(a) Nephogram of horizontal and vertical displacement of the surrounding rock in the C2 stage



(b) Nephogram of transverse and longitudinal displacement of the surrounding rock in the C4 stage

Fig. 14 Cloud map of the surrounding rock displacement field characteristics



(c) Nephogram of transverse and longitudinal displacement of the surrounding rock in the C5 stage

Fig. 14 (continued)

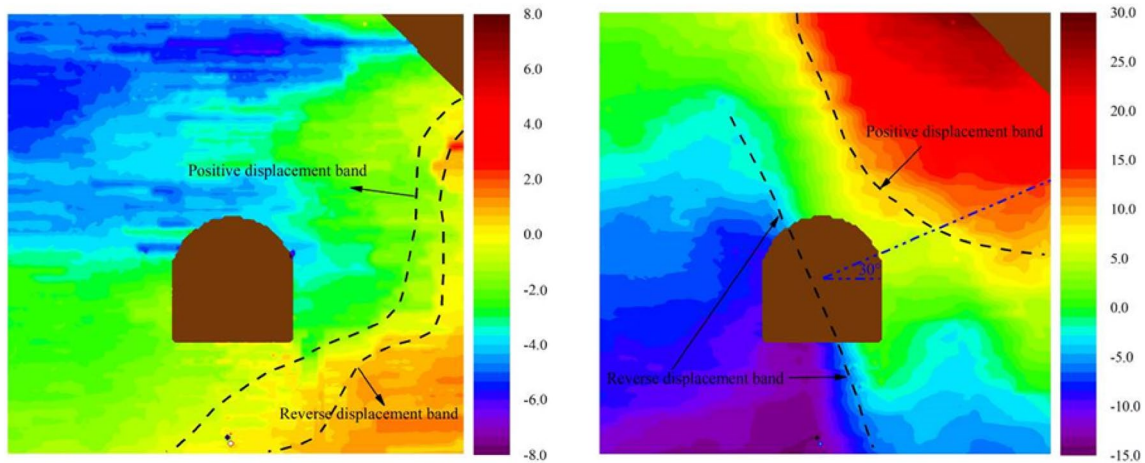


Fig. 15 Displacement model

deformation of this point has the largest values, because it is facing the load application area.

4.4 Strain Analysis of the Tunnel Surrounding Rock

The extraction of the strain slice monitoring data generates the stress field cloud map in the characteristic stage, which can reflect the stress type of the surrounding rock at each point. As shown in Fig. 17, the radial strain cloud map

loaded at the C2 and the C4 stages is utilized to characterize the stress state of the surrounding rock. When the C2 stage is loaded at the 5 min mark, there is a tensile strain zone at the bottom plate of the cavern with a maximum peak micro strain equal to $295 \mu\epsilon$, a tensile strain zone above the roof with a maximum peak strain equal to $185 \mu\epsilon$, and a compressive strain zone at the upper right boundary of the surrounding rock with a maximum strain equal to $2400 \mu\epsilon$, indicating that the area is in a compressive stress state. When loading

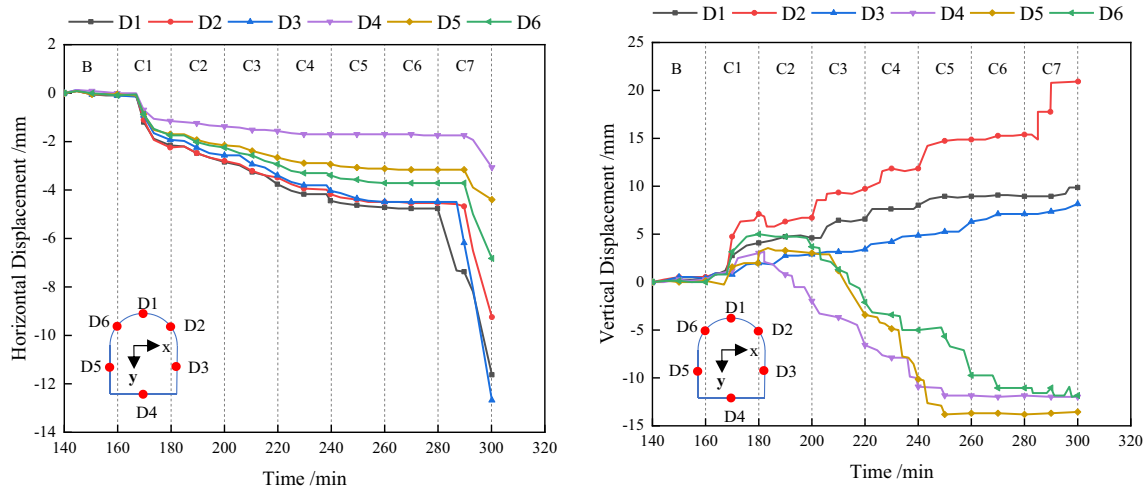


Fig. 16 Displacement monitoring and analysis of the key points

at the 10 min mark, the range of the deep tensile strain zone of the surrounding rock near the bottom plate and the roof is further expanded, and the maximum microstrain is 300 and 230 $\mu\epsilon$. The tensile strain zone appears on the left and right sides of the cavern, and the surrounding rock located distantly from the two sides is in a state of compressive strain. The compressive strain zone spreads to the cavern's center, which tends to surround the tensile strain zone. When the C2 stage is loaded for 20 min, the compressive strain zone surrounds the tensile strain zone, and the tensile strain zone at the bottom plate expands significantly with a peak strain equal to 395 $\mu\epsilon$. When the loading continues to the C4 stage for 5 min, the tensile strain area above the roof accelerates diagonally upward from the left arch waist of the tunnel, and the extension direction points to the asymmetric loading side. The tensile peak strain under the floor increases to 870 $\mu\epsilon$. During the loading process, the tensile strain area near the roof and the free surface of the floor are gradually connected. The upper tensile strain area presents an inverted water drop shape, and the higher tensile strain area at the floor extends to the free surface. During this period, the bottom plate of the tunnel is subjected to tensile stress, and the floor heave is separated.

Based on the obtained results, the distribution characteristics of the strain zone indicate asymmetric characteristics. The free face of the tunnel is prone to early failure at the area defined by large tensile strain. Compared to the measured damage of the model body, it can be observed that the fracture position of the tunnel vault is distributed between the left arch waist and the vault, which confirms the distribution characteristics of the strain field.

4.5 Surrounding Rock Pressure Analysis of the Tunnel Chamber

The monitoring value of the earth pressure box in the surrounding rock model changes with time, as illustrated in Fig. 18. Figure 18a shows the earth pressure box monitoring process in the annular cavern area. It can be observed that the pressure curve of each measuring point generally presents a wave shape. Due to the influence of the initial in-situ stress state during the excavation stage, the balance breaks apart, so the stress value of each measuring point suddenly drops after the 160 min excavation mark. The stress drop of the measuring point above the right arch waist and the roof is minor. As the loading stage proceeds to the C1–C4 stages, the earth pressure values of all measuring points except E1–3 and E1–8 indicate a stepped upward trend. This is explained by the location of the measuring points E1–3 and E1–8 in the surrounding rock area of the roof and the floor. During this interval, the phenomenon of roof subsidence and floor heave occurs in this area, and the separation of the surrounding rock leads to the continuous decrease of the earth pressure box value, in which the earth pressure box value at the floor is close to 0 MPa. It suggests that the surrounding rock failure zone at the bottom plate has spread to 150 mm below the bottom plate. Thus, the surrounding rock failure leads to the instability of this point and cannot transfer the load to the stress surface of the earth pressure box. As the loading continues, the stress at each measuring point begins to decrease around the 240–260 min mark, while the stress at the E1–2 measuring point considerably decreases, because the crack propagation strength of the unit plate continues to

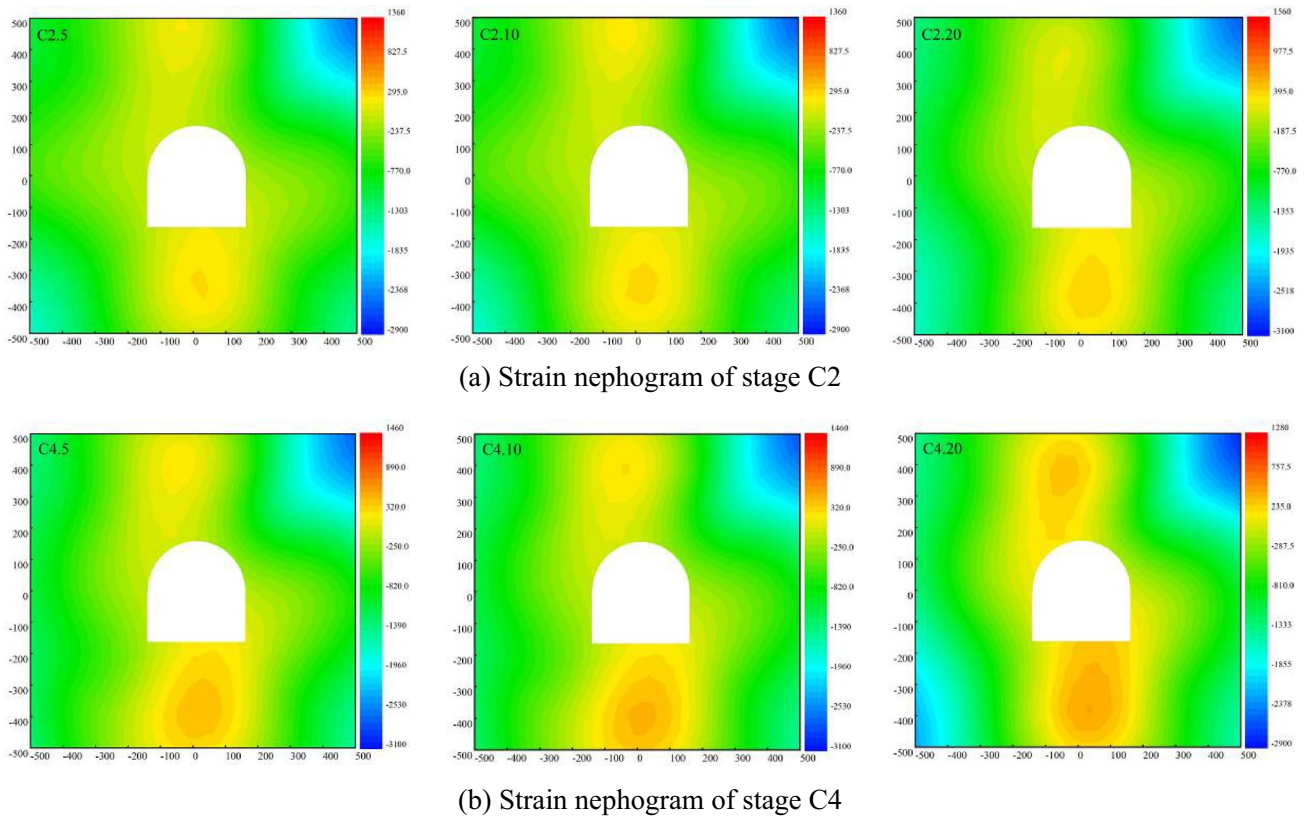


Fig. 17 Model body strain monitoring and analysis

drop and the force acting on the earth pressure box gradually decreases with the loading. The points with high-pressure values in the surrounding area of the tunnel are E1–2, E1–4, E1–7, and E1–9, respectively. The values of points 2 and 9 are higher than points 4 and 7, implying that the surrounding rock pressure on the right side of the tunnel is higher than on the left side. Figure 18b shows the earth pressure box monitoring in the asymmetric loading area. The curve highlights a zigzag trend with a certain degree of similarity and synchronization. The overall pressure of the measuring points E2–1, E2–2, and E2–5 is high, because this area is located close to the uneven pressure release area, far away from the cavern, and the surrounding rock strength is enormous. With the increase of load, the crack extends to the depth of the surrounding rock, points E2–3 and E2–4 are close to the cavern, and the surrounding rock strength is low. Consequently, the pressure value suddenly drops at the 240 min mark.

After performing the analysis, the earth pressure value indicates that the cavern's right side is higher than its left side. In addition, the stress in the asymmetric loading area is higher than in the ring cavern area and gradually decreases along the loading direction.

4.6 Axial Force and Deformation Analysis of the Tunnel Anchor Cable

The axial force of the monitoring anchor cable in the model experiment is extracted, and the monitoring curve of the axial force loading stage is created. At the same time, the displacement and the deformation values of the local measuring points corresponding to the anchor cable anchorage area are compared and analyzed, as shown in (Fig. 20). AC1–AC5 are the anchor cables in the vault area, and AC6–AC11 is the sidewall anchor cables. AC1, AC3, and AC5 serve as the long anchor cables. D1X represents the deformation of the anchor points in the vault area in the horizontal direction.

Figure 19a shows that the axial force of each monitoring anchor cable in the vault area generally is a steady step-by-step upward trend. Simultaneously, a zoning phenomenon occurs, which means that the axial force of the monitoring anchor cables AC1 and AC3 is synchronous and reaches the constant resistance value in the terminal part of the loading stage. In contrast, the axial force of the other anchor cables is asynchronous and does not reach the constant resistance value. This is because the monitoring anchor cables AC1

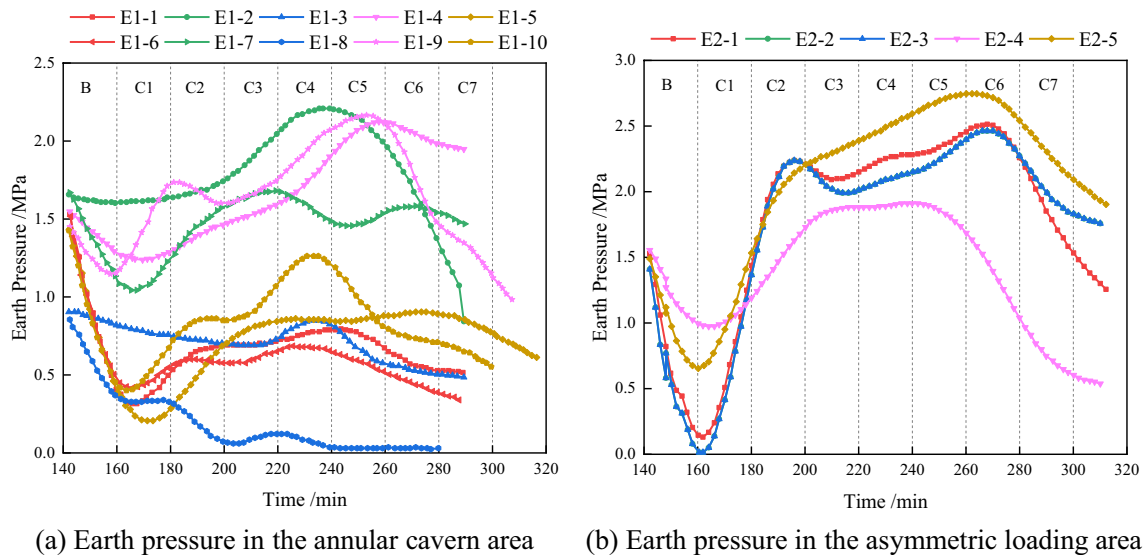


Fig. 18 Earth pressure monitoring and analysis

and AC3 are located in the cavern's middle and right sides and are exposed to asymmetric stress. The surrounding rock in the anchorage range deforms horizontally to the left and vertically downward. The long anchor cable stabilizes the deep surrounding rock and bears a large tension to lock the surrounding rock. Since the anchor cables, AC2 and AC4, are in the gap of the long anchor cable, the stress is shared by the adjacent long anchor cable, which generates a small axial force. In combination with the deformation state of the anchor point at the top plate and the arch waist, it can be observed that the deformation of the anchor point is greatly intensified before and after the 220 min mark. At the same time, the axial force curve of each monitoring anchor cable is accelerated, and then the rising speed of the axial force returns to normal until it is in a stable state.

The axial force of the monitoring anchor cable on the two sides also suggests an upward trend, as illustrated in (Fig. 19b). The axial forces of AC9 and AC10 are synchronous before the 220 min mark, and the axial force of AC10 disappears after the 220 min mark. The fragmentation of the unit plate explains this at the anchor point and the inability to fix the monitoring sensor continuously. The anchor cable AC9 reaches the constant resistance value, while the remaining anchor cables do not reach this value. The deformation of the anchor point accelerates around the 200 min mark. During this period, the axial force curve accelerates at varying degrees, and the rising speed recovers until it is stable.

The obtained results revealed that the monitoring anchor cable in this experiment did not break. The whole loading process accompanies the axial force monitoring curve, which often increases abruptly when the model body begins to deform. Therefore, it can be demonstrated that the

monitoring anchor cable can undertake tunnel deformation monitoring and early warning functions. After the sudden increase of the axial force, the deformation of the anchor point converges and stops growing. At this interval, the axial force of the anchor cable transits from slow growth to a stable state. It proves that the 2G-NPR bolt has energy absorption and buffer characteristics, does not break itself during the process of following the deformation of the surrounding rock, and remains intact when subjected to complex shear action in the surrounding rock deformation. Thus, it accomplishes the integration of support and monitoring.

5 Field Application

5.1 Field Monitoring Equipment

The displacement sensor set on the test site measures the deformation of the surrounding rock. The axial force sensor of the NPR anchor cable is utilized to monitor the supporting load of the anchor cable on the rock wall under the working state. The axial force sensor is installed between the anchor cable tray and the fastening nut. When the force of the anchor cable changes, the force on the axial force sensor between the anchor cable tray and the fastening nut changes correspondingly, causing fiber Bragg grating wavelength change. The pressure change on the anchor cable can be converted by detecting the fiber Bragg grating signal processor, as shown in (Fig. 20).

The NPR anchor bolts/cables field test is conducted at mileage stake YK219 + 504–520 of the Muzhailing tunnel. The material specifications consist of the 1G-NPR anchor

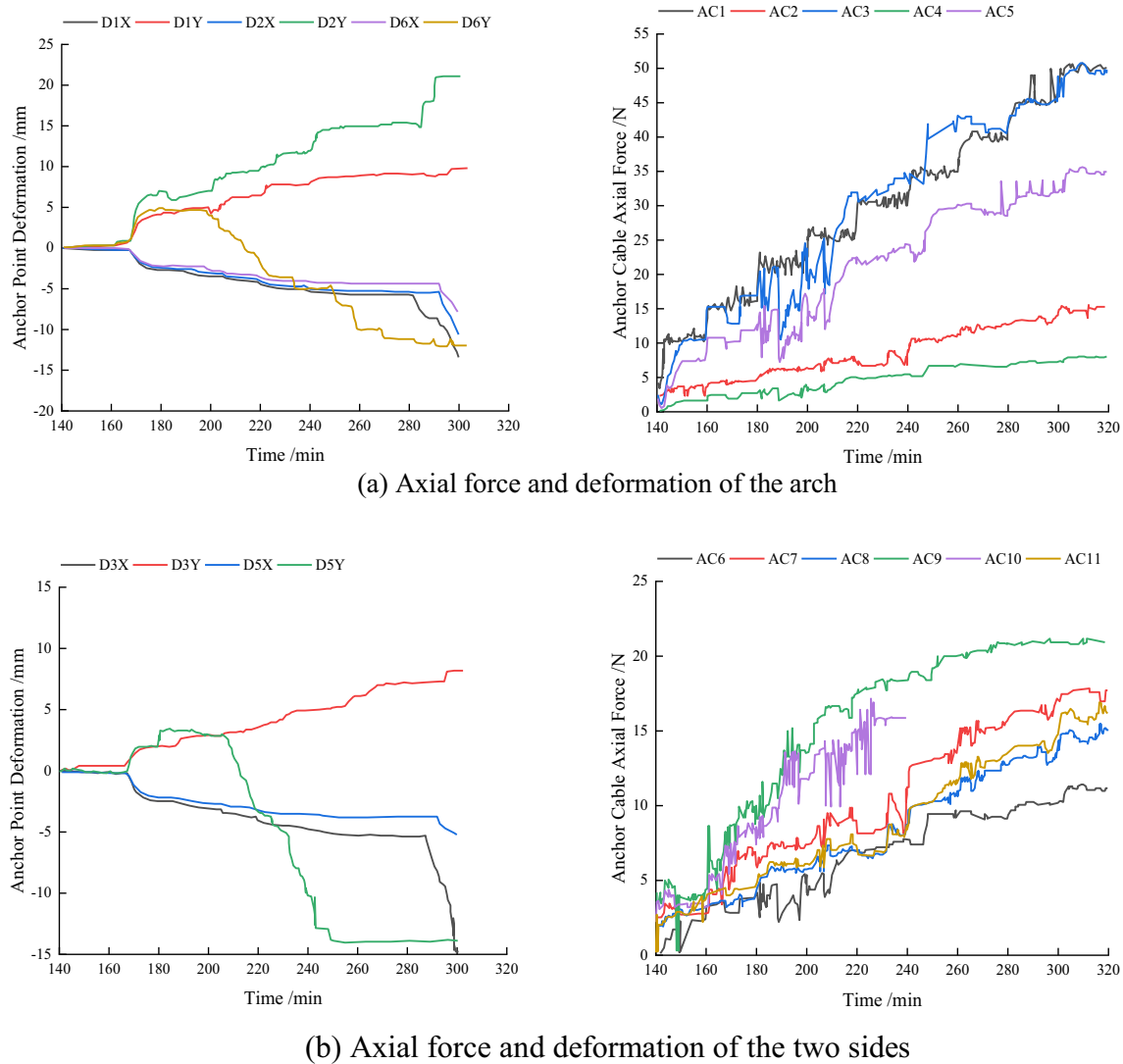


Fig. 19 Axial force of the anchor cable and the tunnel deformation

cable with a 21.8 mm diameter for the long anchor cable and the 2G-NPR anchor bolt with an 18 mm diameter for the short anchor bolt. The main test processes are illustrated in (Fig. 21). The test layout process requires a short time, the timeliness of construction is good, and the preload of a 21.8 mm diameter 1G-NPR anchor cable is 350 kN, and an 18 mm diameter 2G-NPR anchor bolt is 280 kN.

The combined support of the 1G-NPR anchor cable/2G-NPR anchor bolt has achieved favorable control measures of asymmetric large deformation disasters, as shown in (Fig. 22a).

At the same time, the early warning and monitoring equipment is used to monitor the real-time displacement of the critical parts. The convergence of the engineering rock mass after NPR anchor cable support on the project site shows stabilization characteristics in approximately 25 days.

Among them, the displacement of the left shoulder and the vault is large, the other parts are small, and the maximum displacement does not exceed 220 mm and is always below the preset deformation value of 500 mm (Fig. 22b, c). In the experimental model from this study, when the asymmetric seismic damage load is continuously increased, the peak deformation of the surrounding rock under extremely high seismic damage conditions for the C2, C4 to C5 stages is 7, 12, and 13.3 mm, respectively. It is converted into 186.2, 319, and 345.8 mm, respectively, by applying the similarity ratio. The process is below the preset deformation value of 500 mm, indicating that the combined support of the 1G-NPR anchor cable/2G-NPR anchor bolt can demonstrate good energy absorption and extension characteristics under high and extremely asymmetric stress. The deformation of the surrounding rock can be controlled within a safe range.

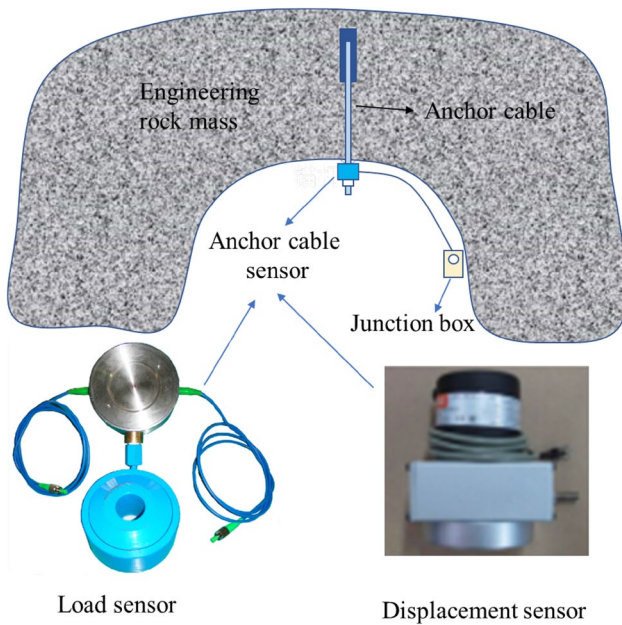


Fig. 20 Field sensor layout

Figure 22d indicates the stress of the anchor cable at the left and right spandrels of the Muzhailing 2# inclined shaft section. When the NPR anchor cable is installed, the force of the anchor cable on the surrounding rock after the arrangement is 290–305 kN due to the loss of preload. With the increase of surrounding rock deformation, the stress on the anchor cable increases. At first, the stress on the anchor cable is linear with the observation time. After reaching its constant resistance value, the stress on the anchor cable floats between 341 and 365 kN. NPR anchor cable rheostat plays a good role in controlling the asymmetric deformation of surrounding rock through an adaptive adjustment with the surrounding rock.

The geomechanical model experiment and field application show that NPR anchor cable has a good constant resistance effect in controlling large asymmetric deformation and

good control and early warning effect for unforeseen engineering deformation.

6 Conclusions

Based on the large-scale geomechanical model test of the Muzhailing tunnel, the damage evolution law, the displacement field, and the strain field of the surrounding rock under asymmetric load are studied in this paper. According to the physical model experiment and the field application effect, the following conclusions can be summarized:

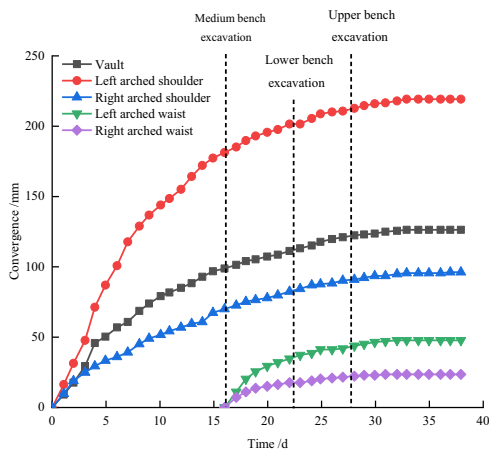
- (1) The failure in the study area represents a parallel or small angle oblique fault mode, leading to severe, non-uniform pressure failure. The upper right corner of the surrounding rock plastic zone indicates that the extension line is parallel to the fault plane, and the extension direction is related to the stress release angle. With the fault dip angle increasing, the stress concentration area on the right side of the surrounding rock moves downward.
- (2) The evolution law of surrounding rock cracks is divided into three stages: incubation, expansion, and overall connection, and the cracks with a width of more than 2 mm gradually spread from the periphery of the tunnel to the oval range at the upper right of the surrounding rock. The displacement field is divided into a positive and reverse displacement zone distributed along the connecting line between the tunnel's left arch waist and the right arch foot.
- (3) The pressure value of the surrounding rock near the tunnel arch crown and right arch waist was greater than that on the left side of the tunnel. There was a tensile strain zone on the bottom plate, and the roof and the tensile strain zone eventually formed an asymmetric butterfly range that was symmetrical around the 30° direction of the first quadrant. The sudden increase



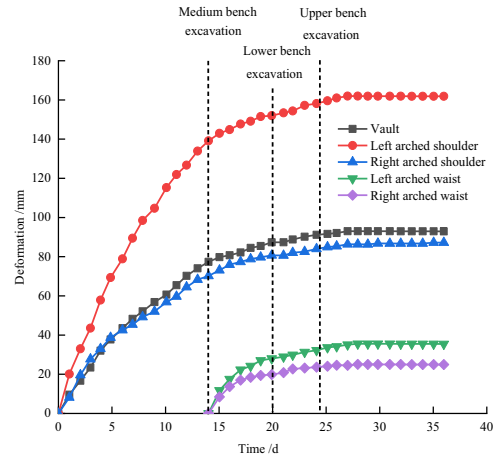
Fig. 21 Stages of the construction process



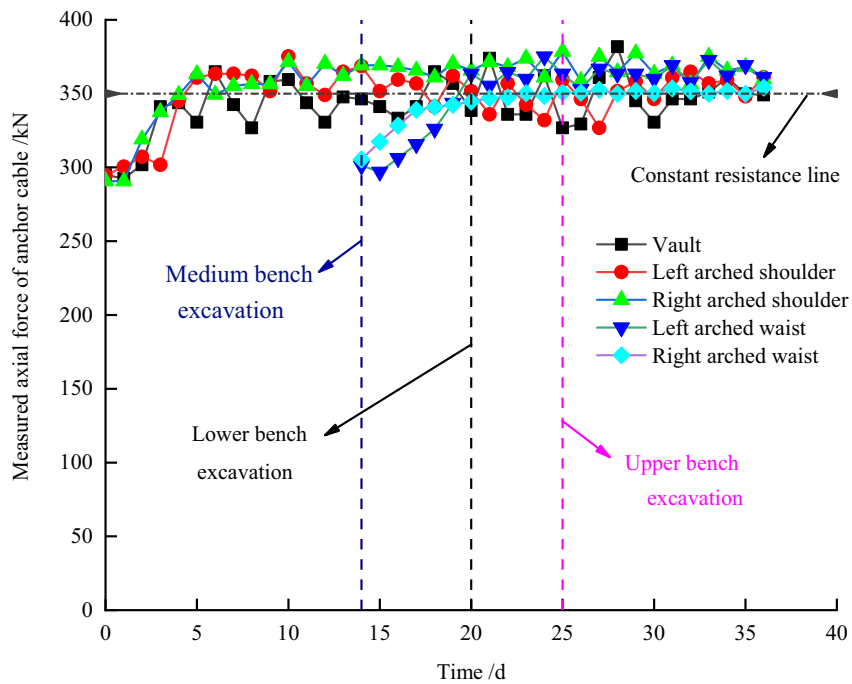
(a) Treatment effect of asymmetric large deformation disaster



(b) Horizontal displacement changes of tunnel



(c) Vertical displacement changes of tunnel



(d) Measured axial force variation curve of anchor cable

Fig. 22 Support results of the NPR anchor cable

of the axial force of the monitoring anchor cable was accompanied by a large deformation of the surrounding rock, which can be used as a monitoring and early warning tool for detecting tunnel deformations.

- (4) The geomechanical model experiment and field application showed that the anchor cable of the model does not break during the deformation process of surrounding rock, which can effectively control the large deformation of surrounding rock and have a good impedance energy absorption effect on crack propagation, forming efficient ductile support under asymmetric load conditions. NPR anchor cable showed a good constant resistance effect in controlling large asymmetric deformation and had reasonable control and early warning effect for unforeseen engineering deformation.

This paper primarily studies the deformation and failure characteristics and the support application of the asymmetric stress in the lower layer slate tunnel. The deformation law of symmetric stress in the lower layer slate tunnel needs further comparative analysis. In addition, the deformation, the failure, and the support countermeasures of asymmetric stress under different influencing factors (including rock stratum angle, lithology, etc.) will be investigated in the future in combination with the numerical model method.

Acknowledgements We would like to thank the anonymous reviewers for carefully reading the manuscript and providing constructive comments to help us improve the quality of this article. This study was supported by the general program of the National Natural Science Foundation of China (approval No. 52074295), the special fund for basic scientific research business expenses of Central Universities (approval No. 2022YJSSB06), and supported by State Key Laboratory for geomechanics and deep underground engineering, China University of Mining and technology, Beijing (approval No. SKLGDUEK202217). We would like to thank MogoEdit (<https://www.mogoedit.com>) for its English editing during the preparation of this manuscript.

Author Contributions WM: conceptualization, data curation, writing—original draft. XY: supervision, funding acquisition. WZ: writing—review and editing, software, formal analysis. CZ: project administration, resources. YM: writing—review and editing, software. XW: visualization, data curation. MH: supervision, methodology. ZT: visualization, validation.

Funding The National Natural Science Foundation of China (approval No. 52074295). The special fund for basic scientific research business expenses of Central Universities (approval No. 2022YJSSB06). State Key Laboratory for geomechanics and deep underground engineering, China University of Mining and technology, Beijing (approval No. SKLGDUEK202217).

Declarations

Conflict of Interest The authors declare that they have no known competing financial interests or personal relationships that could have appeared to influence the work reported in this paper.

References

- Aydan O, Akagi T, Kawamoto T (1993) The squeezing potential of rocks around tunnels: theory and prediction. *Rock Mech Rock Eng* 26(2):137–163. <https://doi.org/10.1007/BF01023620>
- Chen ZJ (1982) The mechanical problems for the long-term stability of underground galleries. *Chinese J Rock Mech Eng* 1(1):1–20
- Chen Z, He C, Xu G, Ma G, Wu D (2019) A case study on the asymmetric deformation characteristics and mechanical behavior of deep-buried tunnel in phyllite. *Rock Mech Rock Eng* 52:4527–4545. <https://doi.org/10.1007/s00603-019-01836-2>
- Chen DG, Zhaoning G, Li SS (2020a) Analysis of elastic surrounding rock stress of circular tunnel under non-uniform stress field. *Sci Technol Eng* 20:8791–8797 (in Chinese with English Abstract)
- Chen Z, He C, Yang W, Guo W, Li Z, Xu G (2020b) Impacts of geological conditions on instability causes and mechanical behavior of large-scale tunnels: a case study from the Sichuan-Tibet highway. *China b Eng Geol Environ* 79:3667–3688. <https://doi.org/10.1007/s10064-020-01796-w>
- Chen Y, Li L, Zhou Z, Tu W, Zhu Y, Shang C (2021) Asymmetric deformation characteristics and support scheme design of the surrounding rock in deep roadway. *Arab J Geosci*. <https://doi.org/10.1007/s12517-021-06837-6>
- Guo Z, Fan J, Wang F, Zhou H, Li W (2021) Geomechanical model experiment study on deformation and failure mechanism of the mountain tunnel in layered jointed rock mass. *Adv Civil Eng* 2021:1–19. <https://doi.org/10.1155/2021/6645124>
- Hou D, Yang X (2018) Physical modeling of displacement and failure monitoring of underground roadway in horizontal strata. *Adv Civil Eng* 2018:1–11. <https://doi.org/10.1155/2018/2934302>
- Hu X, He C, Walton G, Chen Z (2020) A combined support system associated with the segmental lining in a jointed rock mass: the case of the inclined shaft tunnel at the Bulianta coal mine. *Rock Mech Rock Eng* 53:2653–2669. <https://doi.org/10.1007/s00603-020-02056-9>
- Lei M, Peng L, Shi C (2015) Model test to investigate the failure mechanisms and lining stress characteristics of shallow buried tunnels under unsymmetrical loading. *Tunn Undergr Sp Tech* 46:64–75. <https://doi.org/10.1016/j.tust.2014.11.003>
- Lin P, Shi J, Zhou W, Wang R (2018) 3D geomechanical model tests on asymmetric reinforcement and overall stability relating to the Jinping I super-high arch dam. *Int J Rock Mech Min* 102:28–41. <https://doi.org/10.1016/j.ijrmm.2017.11.017>
- Liu D, Li M, Zuo J, Gao Y, Zhong F, Zhang Y, Chang Y (2021) Experimental and numerical investigation on cracking mechanism of tunnel lining under bias pressure. *Thin Wall Struct* 163:107693. <https://doi.org/10.1016/j.tws.2021.107693>
- Peng R, Meng X, Zhao G, Ouyang Z, Li Y (2021) Multi-echelon support method to limit asymmetry instability in different lithology roadways under high ground stress. *Tunn Undergr Sp Tech* 108:103681. <https://doi.org/10.1016/j.tust.2020.103681>
- Qi X, Wang R, Mi W (2020) Failure characteristics and control technology of surrounding rock in deep coal seam roadway with large dip angle under the influence of weak structural plane. *Adv Civil Eng* 2020:1–17. <https://doi.org/10.1155/2020/6623159>
- Sun X, Chen F, He M, Gong W, Xu H, Lu H (2017) Physical modeling of floor heave for the deep-buried roadway excavated in ten degree inclined strata using infrared thermal imaging technology. *Tunn Undergr Sp Tech* 63:228–243. <https://doi.org/10.1016/j.tust.2016.12.018>
- Sun X, Chen F, Miao C, Song P, Li G, Zhao C, Xia X (2018) Physical modeling of deformation failure mechanism of surrounding rocks for the deep-buried tunnel in soft rock strata during the excavation. *Tunn Undergr Sp Tech* 74:247–261. <https://doi.org/10.1016/j.tust.2018.01.022>

- Ta X, Wan Z, Zhang Y, Shi P, Wei Z, Sun X, Jia L (2021) Field and numerical investigation on the coal pillar instability of gob-side entry in gently inclined coal seam. *Adv Civil Eng* 2021:1–12. <https://doi.org/10.1155/2021/4901670>
- Tao Z, Zhu C, He M, Karakus M (2021) A physical modeling-based study on the control mechanisms of negative poisson's ratio anchor cable on the stratified toppling deformation of anti-inclined slopes. *Int J Rock Mech Min* 138:104632. <https://doi.org/10.1016/j.ijrmms.2021.104632>
- Vitali OPM, Celestino TB, Bobet A (2019) Shallow tunnels misaligned with geostatic principal stress directions: analytical solution and 3D face effects. *Tunn Undergr Sp Tech* 89:268–283. <https://doi.org/10.1016/j.tust.2019.04.006>
- Wang SR, Liu ZW, Qu XH, Fang JB (2009) Large deformation mechanics mechanism and rigid-gap-flexible-layer supporting technology of soft rock tunnel. *China J Highway Trans* 22(6):90–95. [https://doi.org/10.1016/S1874-8651\(10\)60059-2](https://doi.org/10.1016/S1874-8651(10)60059-2)
- Wu G, Chen W, Jia S, Tan X, Zheng P, Tian H, Rong C (2020) Deformation characteristics of a roadway in steeply inclined formations and its improved support. *Int J Rock Mech Min* 130:104324. <https://doi.org/10.1016/j.ijrmms.2020.104324>
- Xiong X, Dai J, Chen X (2020) Analysis of stress asymmetric distribution law of surrounding rock of roadway in inclined coal seam: a case study of Shitanjing No. 2 coal seam. *Adv Civil Eng* 2020:1–14. <https://doi.org/10.1155/2020/8877172>
- Xu X, He F, Li X, He W (2021) Research on mechanism and control of asymmetric deformation of gob side coal roadway with fully mechanized caving mining. *Eng Fail Anal* 120:105097. <https://doi.org/10.1016/j.engfailanal.2020.105097>
- Yang X, Jing H, Tang C, Yang S (2017) Effect of parallel joint interaction on mechanical behavior of jointed rock mass models. *Int J Rock Mech Min* 92:40–53. <https://doi.org/10.1016/j.ijrmms.2016.12.010>
- Yang S, Chen M, Fang G, Wang Y, Meng B, Li Y, Jing H (2018) Physical experiment and numerical modelling of tunnel excavation in slanted upper-soft and lower-hard strata. *Tunn. Undergr Sp Tech* 82:248–264. <https://doi.org/10.1016/j.tust.2018.08.049>
- Yu Q, Song Z, Du C, Dai Z, Yin S, Soltanian MR, Soltanian M, Liu W (2020) Analysis of asymmetric stress ratio in shallow buried tunnels. *KSCE J Civ Eng* 24:1924–1931. <https://doi.org/10.1007/s12205-020-2063-1>
- Zhang B, Zhou H, Chang Q, Zhao X, Sun Y (2020) The stability analysis of roadway near faults under complex high stress. *Adv Civil Eng* 2020:1–10. <https://doi.org/10.1155/2020/8893842>
- Zhao Y, Shi Y, Yang J (2019) Cracking of tunnel bottom structure influenced by carbonaceous slate stratum. *Mag Civil Eng* 86(2):83–91. <https://doi.org/10.18720/MCE.86.8>
- Zheng H, Li P, Ma G (2021) Stability analysis of the middle soil pillar for asymmetric parallel tunnels by using model testing and numerical simulations. *Tunn Undergr Sp Tech* 108:103686. <https://doi.org/10.1016/j.tust.2020.103686>
- Zheng H, Li P, Ma G, Zhang Q (2022) Experimental investigation of mechanical characteristics for linings of twins tunnels with asymmetric cross-section. *Tunn Undergr Sp Tech* 119:104209. <https://doi.org/10.1016/j.tust.2021.104209>

Publisher's Note Springer Nature remains neutral with regard to jurisdictional claims in published maps and institutional affiliations.

Springer Nature or its licensor holds exclusive rights to this article under a publishing agreement with the author(s) or other rightsholder(s); author self-archiving of the accepted manuscript version of this article is solely governed by the terms of such publishing agreement and applicable law.